Enhancing AA7075 Spot Welding with Multipulsed Current and Magnetic Fields: Part 1 — Materials Characterization

Suppressing hot cracking, inhibiting porosity defects, and refining the grains through a new composite process

BY Z. LI, Z. TENG, J. CHEN, J. QUEVAL, C. QIAN, J. BROWN, Y. XIA, AND Y. LI

Abstract

High-strength, corrosion-resistant, and heat-treatable 7xxx aluminum alloys have long been important structural materials in the aerospace industry. Recently, driven by the progress in vehicle lightweighting, the application of 7xxx aluminum alloys has also emerged as a prevailing trend in high-speed rail and automotive manufacturing. However, welding 7xxx aluminum alloys with high-alloying-element content presents stubborn porosity and hot-cracking defects. The magnetically assisted resistance spot welding (MA-RSW) process has been proven to be an effective method to improve the toughness of aluminum alloy welds by introducing electromagnetic stirring. Still, it may increase the risk of expulsion. In response to these challenges, this two-part paper aims to investigate a composite process called multipulsed magnetically assisted resistance spot welding (MPMA-RSW), which combines an external magnetic field and a multipulse current schedule to improve the weldability of 7xxx sheets. This part compares material characterization using different methods, including nugget appearance, microstructure, and crack propagation. The results show that both the multipulsed resistance spot welding and the MA-RSW processes can inhibit the porosity defects but cannot avoid hot cracking. In contrast, the composite process MPMA-RSW can effectively inhibit the porosity defects, reduce the hot cracks, and refine the grains. The MPMA-RSW process can be used to address the welding challenges of 7xxx aluminum alloys, presenting a favorable outlook for industrial applications.

https://doi.org/10.29391/2025.104.020

Keywords

- 7xxx Aluminum Alloys
- Resistance Spot Welding
- Magnetically Assisted
- Multipulse Current
- Grain Size

Introduction

Aluminum alloys, renowned for their lightweight properties and high strength-to-weight ratio, are pivotal in modern manufacturing, especially in the automotive and aerospace industries (Ref. 1). Among these alloys, AA7075 stands out for its exceptional strength, corrosion resistance, a broad spectrum of solution heat treatment temperatures, and rapid natural aging properties (Ref. 2). However, as a kind of the Al-Zn-Mg-Cu series, AA7075 holds a substantial amount of alloying elements, exhibits a wide melting range with a low solidus temperature, and is highly prone to weld cracking (Ref. 3), making AA7075 a "non-weldable" alloy (Ref. 4). With the rise of friction stir welding (FSW), solid-phase bonding has become a novel approach to solving the problem of AA7075 welding (Ref. 5). For pipe or rod welding, rotary friction welding (RFW) has emerged as a promising solid-state joining method for reliably connecting materials with high hot cracking sensitivity (Ref. 6). Nevertheless, due to cost and efficiency considerations, conventional welding methods have been extensively studied over the past few decades and have not been abandoned.

Many efforts have been dedicated to obtaining effective fusion joints for AA7075. Zhang et al. investigated double-wire pulsed cold metal transfer welding, achieving a maximum strength of 63% compared to the base material (BM) strength for 6 mm AA7075-T6 welds without postweld heat treatment (PWHT) (Ref. 7). Liu et al. studied the sinu-

Table 1 — Chemical Composition (wt-%) of AA7075

Grade	Zn	Mg	Cu	Cr	Fe	Si	Al
AA7075	5.787	2.47	1.73	0.20	0.20	0.10	Bal.

Fig. 1 — Welding system.

soidal oscillating laser welding of AA7075 and studied the dynamics of the weld pool and mechanisms for suppressing porosity defects through simulation. The results show that oscillating frequency optimization reduced the porosity rate to only 1% (Ref. 8). Hu et al. (Ref. 9) proposed a hybrid welding strategy exploiting laser beam oscillation and a pulsed magnetic field in hybrid laser and arc butt weld of AA7050 and increased the tensile strength to ~90% compared to the BM. The researchers underscored the positive impact of the pulses, oscillations, or external magnetic fields, mainly controlling the thermal evolution and the fluid flow, which have become the common methods to improve the fusion welding quality of 7-series aluminum alloys.

Resistance spot welding (RSW) is the leading process in body manufacturing due to its low cost, high degree of automation, and strong adaptability. Applying an external magnetic field in the RSW process, called the magnetically assisted RSW (MA-RSW) process, has been widely studied since 2011 (Ref. 10), which can reduce defects and refine grains in aluminum welding (Ref. 11). Qi et al. applied MA-RSW to A7N01. They effectively increased the fatigue life of the joint by approximately 137.31% and 60.71% under low-load and high-load conditions (Ref. 12), respectively. However, MA-RSW, to some extent, increases the risk of expulsion during the welding process (Ref. 13). It is crucial to set appropriate parameters to suppress expulsion (Ref. 14). Li et al. (Refs. 15, 16) successfully optimized the MA-RSW process by employing step-pulse parameters. To improve the quality of aluminum welding, General Motors (GM) developed a multipulsed (MP) RSW parameter called the conditioning, shaping, and sizing (CSS) schedule (Ref. 17), which was utilized by Deng et al. to obtain defect-free aluminum alloy joints (Ref. 18). Therefore, introducing MP-RSW parameters into the MA-RSW process could be a viable measure to address the expulsion issue.

This study addressed the poor weldability of hot-stamped 7075 aluminum alloy by combining the MA and MP methods to propose a composite process called MPMA-RSW for solving the persistent AA7075 welding defects. Two companion papers were presented to summarize this study and validate the effectiveness of MPMA-RSW. Each part introduced individual processes — RSW, MA-RSW, and MP-RSW — separately for comparison. In the RSW and MA-RSW control groups, single-pulse welding parameters were used. In part 1, a comprehensive analysis of macro and micro morphologies was conducted for each process combination: traditional RSW, MP-RSW, MA-RSW, and MPMA-RSW. In Part 2, the mechanisms to suppress expulsion and the mechanical properties were studied. Results indicated that, due to the combined effects of the comprehensive regulation of heat and mass transfer from MP and MA, the MPMA-RSW process can make welds with fewer defects and superior performance.

Experimental Procedures

Materials

The study utilized 2.8 mm-thick hot-stamped 7075 aluminum alloy sheets, which have been processed through artificial aging to achieve the T6 condition, with the chemical composition listed in Table 1. All workpieces were manufactured with dimensions of 150 × 50 mm and underwent alcohol cleaning prior to welding. The overlap width between the two sheets was 50 mm.

Welding Process

The welding tests were executed on a Fanuc R2000iC robot, a mid-frequency direct current (MFDC) welding controller made by Welding Technology Corp. (WTC), and a Centerline C-gun for resistance spot welding, as shown in Fig. 1. The design of the C-gun resembles the letter ‘C’ and is suitable for applications requiring high welding pressure. The GM-patented multiring domed (MRD) electrode was used to disrupt oxide films on the aluminum sheet surface, resulting in a notable reduction in contact resistance between the aluminum sheet and electrode (Refs. 19, 20).

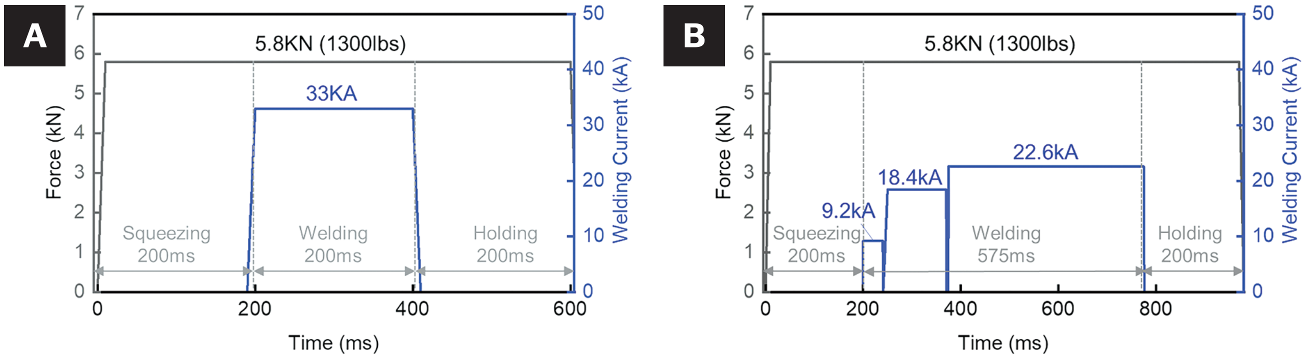

Fig. 2 — Welding schedule: A — The RSW schedule; B — the RMS value of the multipulsed schedule.

This study employed four different process combinations: RSW, utilizing single-pulse parameters without an external magnetic field; MA-RSW, using single-pulse parameters with the addition of an external magnetic field; MP-RSW, employing multipulse parameters without an external magnetic field; and MPMA-RSW, utilizing multipulse parameters and incorporating an external magnetic field.

As shown in Fig. 2A, the RSW and MA-RSW processes adopted single-pulse welding parameters at 33 kA. The welds produced with the adopted single-pulse parameters meet the requirements of AWS D8.2M standards, ensuring that the nugget diameter exceeds 7 mm (Ref. 21). The MP-RSW parameter was designed with reference to the patented CSS weld schedule (Ref. 17). The conditioning stage was intended to break surface oxides of aluminum sheet to focus the heat generation on the faying interface; the shaping stage shaped the aluminum weld nugget at the faying interface, while the sizing stage promoted the growth of the nugget (Ref. 18). Each stage consisted of several designed current pulses of different durations and intensities.

The MP-RSW and MPMA-RSW welds, as shown in Fig. 2B, were produced at an electrode force of 1300 lb (5.8 kN), and the initial conditioning stage was 9.2 kA root-mean-square (RMS) for 0.04 s followed by 0.01 s of cooling. Then, the shaping stage was 18.4 kA RMS for 0.12 s, followed by 0.01 s of cooling. The sizing stage was 22.6 kA RMS applied over 0.40 s followed by the holding period of 0.20 s to achieve weld solidification, as shown in Fig. 2B. To facilitate comparison, the single and MP-RSW parameters were designed to make similar nugget diameters.

For the magnetically assisted (MA) method, encompassing both the MA-RSW and MPMA-RSW processes, circular N52 permanent magnets were attached to both the upper and lower electrodes, as depicted in Fig. 3. The circular permanent magnets were 10 mm in height, with outer and inner diameters of 34 and 24 mm, respectively. The distance between the permanent magnet and the workpiece was 3 mm. Figure 3 illustrates the radial magnetic flux density measured using the TUNKIA TM5100 series Gauss meter and the test method aligned with previous studies (Ref. 22).

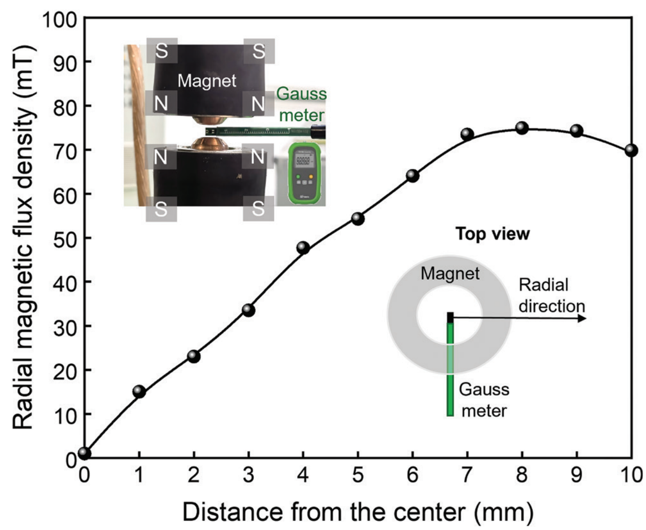

Fig. 3 — External magnetic field distribution.

Characterization and Testing

The cross-sectioned samples underwent wire cutting, followed by cold embedding with acrylic powder, and grinding and polishing using standard metallographic procedures to 0.05 µm by silica polishing liquid. Keller's reagent was applied to etch the welded joints, facilitating the visualization of macrostructures and microstructures. Nugget profiles were observed using a Leica DFC295 digital optical microscope (O.M.). A Leica DM4M was used for higher magnification. A TESCAN MIRA3 scanning electron microscope (SEM) with electron backscattering diffraction (EBSD) capabilities was utilized for further microstructure analysis. The operating voltage for EBSD was 20 kV. The step size for EBSD images at a magnification of 500X was 3 µm, while the step size for images at a magnification of 2500X was 0.6 µm. EBSD data postprocessing was performed using AZtecCrystal software without employing any data clean-up procedures.

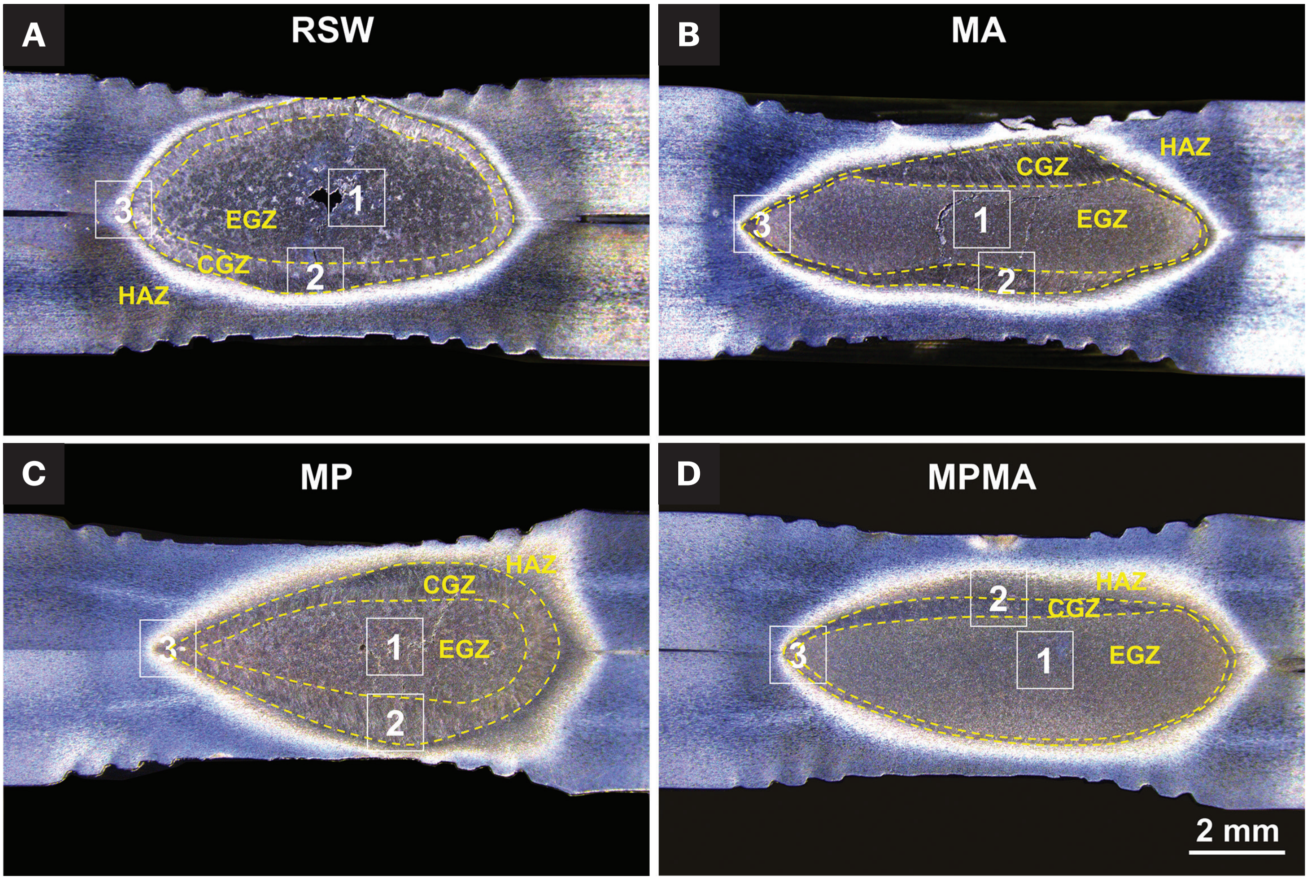

Fig. 4 — Nugget geometry for AA7075 welds: A — RSW; B — MA-RSW; C — MP-RSW; D — MPMA-RSW (CGZ: Columnar Grain Zone, EGZ: Equiaxed Grain Zone, HAZ: Heat-Affected Zone).

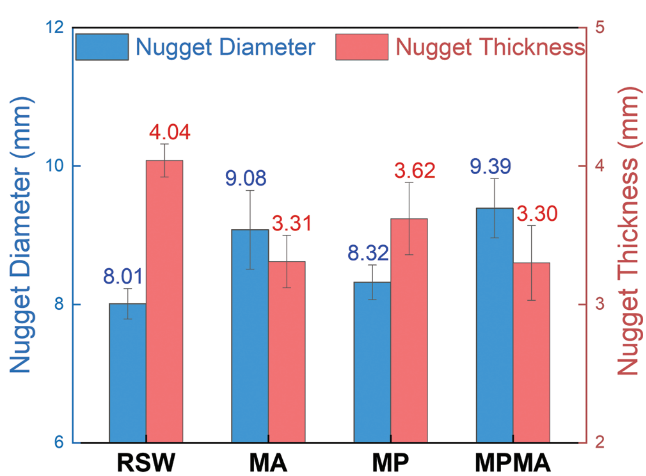

Fig. 5 — Nugget diameter and thickness comparison.

Results

Nugget Appearance

Figure 4 displays the nugget morphology observed under an optical microscope for each welding process. Due to the utilization of the MRD electrode cap, the sheet and the electrode contact surfaces exhibited serrated depressions. When observing the relative position of the nugget within the weld, RSW exhibited significant upward deviation, with the molten pool reaching the outer surface of the sheet. In contrast, MP-RSW displayed substantial rightward deviation. However, MA-RSW and MPMA-RSW showed much less deviation, indicating that an external magnetic field can ameliorate nugget deviation. Examining the defect aspect, RSW showed pronounced voids and crack defects, while MA-RSW and MP-RSW had no significant voids but exhibited cracks. Under the magnification used in Fig. 4, MPMA-RSW exhibited no significant defects. However, the stratification in MPMA-RSW was less severe than in MA-RSW. In terms of the nugget size, MP-RSW, obtained with multipulse parameters, and RSW, with single-pulse parameters, had similar nugget diameters. However, the nugget obtained with RSW had a larger thickness, posing a higher risk of complete joint penetration. With an external magnetic field, MA-RSW and MPMA-RSW increased

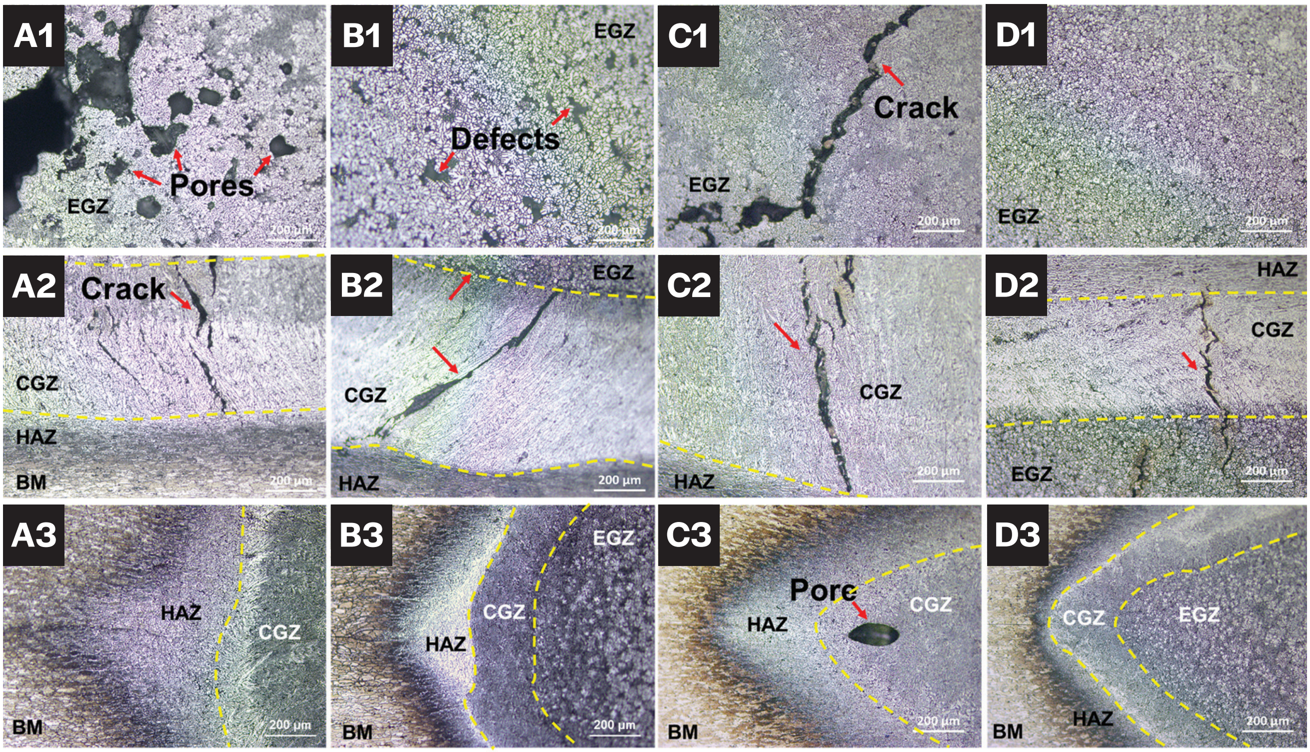

Fig. 6 — Enlarged O.M. photographs of AA7075 nugget. A1~A3 correspond to the region 1~3 marked in Fig. 4A; B1~B3 correspond to the region 1~3 marked in Fig. 4B; C1~C3 correspond to the region 1~3 marked in Fig. 4C; D1~D3 correspond to the region 1~3 marked in Fig. 4D.

the nugget diameter by 13.4% and 12.9% while reducing the thickness by 18.1% and 8.84%, compared to RSW and MP-RSW, respectively, as shown in Fig. 5.

Microstructure

In the center of the nugget, the AA7075 RSW, MA-RSW, and MP-RSW exhibited significant shrinkage, void defects, and penetrating cracks, while the MPMA-RSW process eliminated almost all defects. Additionally, in the nugget center, MA-RSW displayed numerous small defects akin to insufficient filling (see Fig. 6B1). In contrast, the MPMA-RSW process, while manifesting this phenomenon, presented smaller and more dispersed defects (see Fig. 6D1) due to the grain refinement. The remelting during the MP-RSW process may contribute to eliminating defects (Ref. 23). Under various process parameters, columnar grain zones (CGZs) along the fusion boundary exhibited predominantly intergranular cracks, often originating from liquation cracks in the HAZ, as shown in Figs. 6A2, B2, C2, and D2.

The nugget can be divided into the CGZ and the equiaxed grain zone (EGZ). After etching, etching marks appeared in the interdendritic spaces of the aluminum alloy. The grains in the CGZ typically exhibit a narrow, columnar morphology, while those in the EGZ are uniform and equiaxed, lacking a distinct orientation. Due to the small size of the dendrites and the high density of etch marks, the EGZ often appears darker under an optical microscope, as shown in Fig. 6. This difference manifests as a variation in color contrast under low magnification (Fig. 4). Because of the important role of the CGZ in crack initiation, it was very important to study the size and morphology of the CGZ in different processes. Macroscopically and in conjunction with Fig. 4, it was evident that both MP-RSW and MA-RSW resulted in wider CGZs, whereas the RSW and MPMA-RSW processes yielded narrower EGZs. Consequently, cracks within the columnar grains were relatively finer and shorter in MPMA-RSW nuggets.

The Grain Morphology in Nugget

In the schematic diagrams along the top of Fig. 7, the EBSD mapping areas are indicated by white frames, with each region containing the CGZ, EGZ, and cracks. The cracks were located along high-angle grain boundaries (HAGBs) and were predominantly distributed in the EGZ and CGZ. However, as shown in Fig. 7D, the hot cracks in the EGZ of MPMA-RSW were relatively small.

The average length-to-width ratio for the CGZ followed the sequence: MPMA-RSW (4.67) > MP-RSW (3.74) > RSW (2.66) > MA-RSW (2.23). The columnar grains of MPMA-RSW were the narrowest. Compared with the BM, the grain size of the columnar grain grew significantly. The average width of the columnar grain in RSW, MA-RSW, and MP-RSW was about 30 μm, with high standard deviations, as shown in Fig. 8A. The average width of the MPMA-RSW columnar grain was lower than that of other processes (25.9 μm), with a standard deviation of only 14.0 μm. The CGZ of MA-RSW exhibited numerous fine equiaxed grains, whereas, in the CGZ of other composite processes, only a few fine equiaxed grains were present. As shown in Fig. 8B, the grain size of

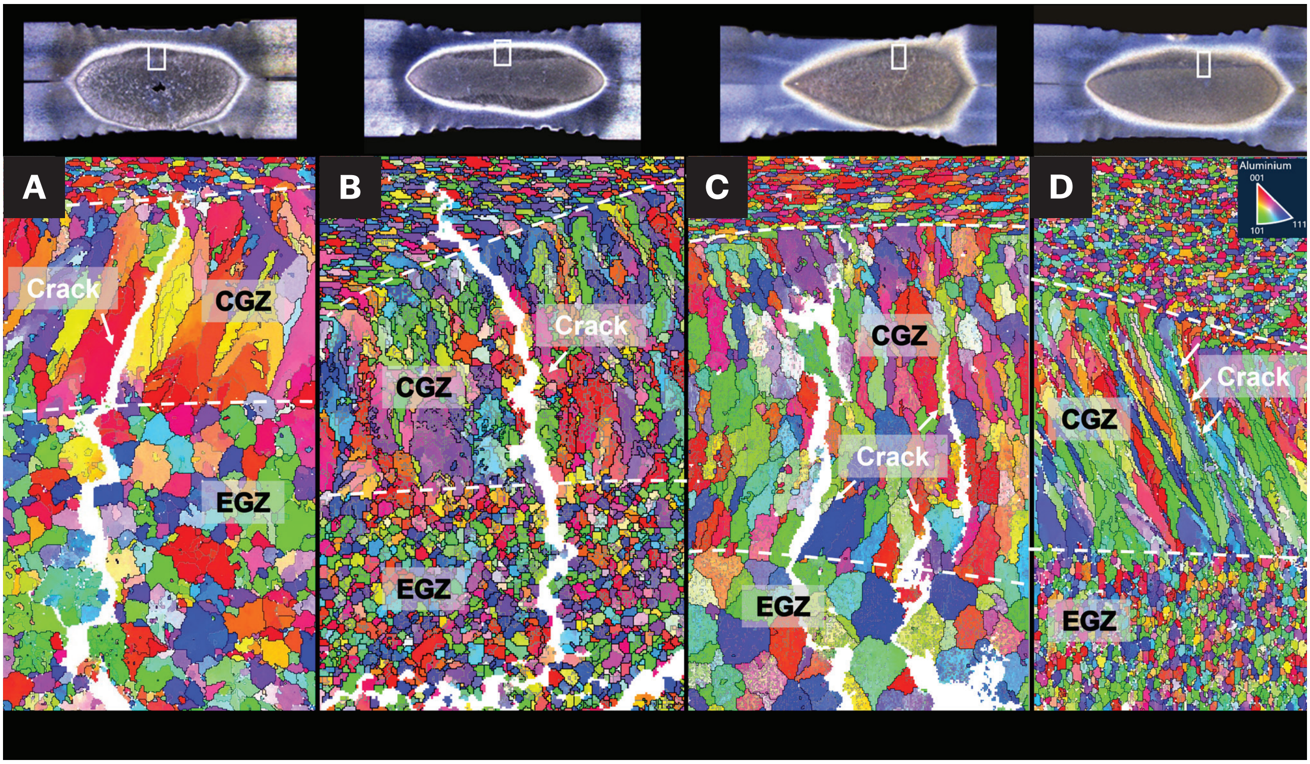

Fig. 7 — The EBSD analysis of CGZs and their surrounding areas: A — RSW; B — MA-RSW; C — MP-RSW; D — MPMA-RSW.

the EGZ in RSW and MP-RSW was similar, around 30 µm, while for MA-RSW and MPMA-RSW, it was greatly reduced by 57.4% and 63.3%, respectively.

Discussion

The Formation of the Macrostructure

As shown in Fig. 4, among the four processes of RSW, MP-RSW, MA-RSW, and MPMA-RSW, RSW exhibited an upward shift in the nugget growth; MP-RSW showed a significant lateral shift in the nugget growth, while MA-RSW demonstrated notable nugget stratification. The upward growth of the RSW nugget was primarily due to the Peltier effect, where heat absorption and release occurred as the current flowed through different media (Ref. 24). The principle of the Peltier effect lies in the difference in energy levels of electrons in various materials. When electrons move from a higher energy level to a lower one, energy is released in the form of heat (Ref. 25). The energy level of electrons in aluminum is higher than that in copper (Ref. 26). Consequently, when electrons move from an aluminum alloy to a copper electrode, heat is released. Conversely, heat is absorbed when electrons move from copper to aluminum. Therefore, the positive electrode releases heat while the negative electrode absorbs heat, which results in an overheating of the sheet in contact with the positive electrode during welding. The morphology of the MP-RSW nugget was attributed to the uneven oxide layer on the aluminum alloy surface. When using C-gun welding, due to the deflection of the welding gun, the conductive path was asymmetrical (Ref. 27). Moreover, the characteristics of a low current and long time of MP-RSW parameters facilitated the displacement of the nugget towards the outside of the welding gun, which was more likely to cause expulsion. Given the high heat generation at the interface, the nugget thickness increased rapidly during the initial welding phase, followed by a gradual decrease as the welding process continued (Ref. 28). As the nugget diameter increased, electromagnetic stirring intensified, causing the nugget's diameter to grow faster (Ref. 29), while its thickness decreased. The previously melted regions gradually solidify during this process, forming a coarser CGZ. The rapid circumferential flow was induced by electromagnetic stirring, which significantly reduced the temperature gradient in the nugget center, resulting in a nearly simultaneous solidification mode for the central EGZ (Ref. 30). In summary, MPMA-RSW combined the advantages of both processes, mitigating their disadvantages. The circumferential flow induced by MA corrected the nugget shift caused by MP, while the repeated remelting and heating by MP corrected the nugget stratification caused by MA, resulting in a well-formed nugget.

The Formation of the Microstructure

A greater number of fine equiaxed grains in CGZ of MA-RSW is consistent with the findings of Qi et al. (Ref. 12) in the MA-RSW of A7N01 aluminum alloy, which may be related to the change in the flow pattern within the nugget of MA-RSW. Under the influence of an external magnetic field, a 3D compound flow is generated within the nugget of aluminum alloy spot welding. As a result, the nugget flow velocity is increased to five times that of conventional spot welding, as shown in Fig. 9 (Ref. 31). The high-speed inertial flow disrupts the growth of columnar dendrites, thereby promoting the formation of new heterogeneous nuclei (Ref. 32). Analysis of the grain size distribution in Fig. 8A reveals a higher percentage of grains smaller than 20 μm in MPMA-RSW compared with MA-RSW, suggesting that the multipulse technique may intensify the flushing effect of molten metal on the CGZ. Due to the narrow and elongated features of the grains in the CGZ of MPMA-RSW, the presence of fine

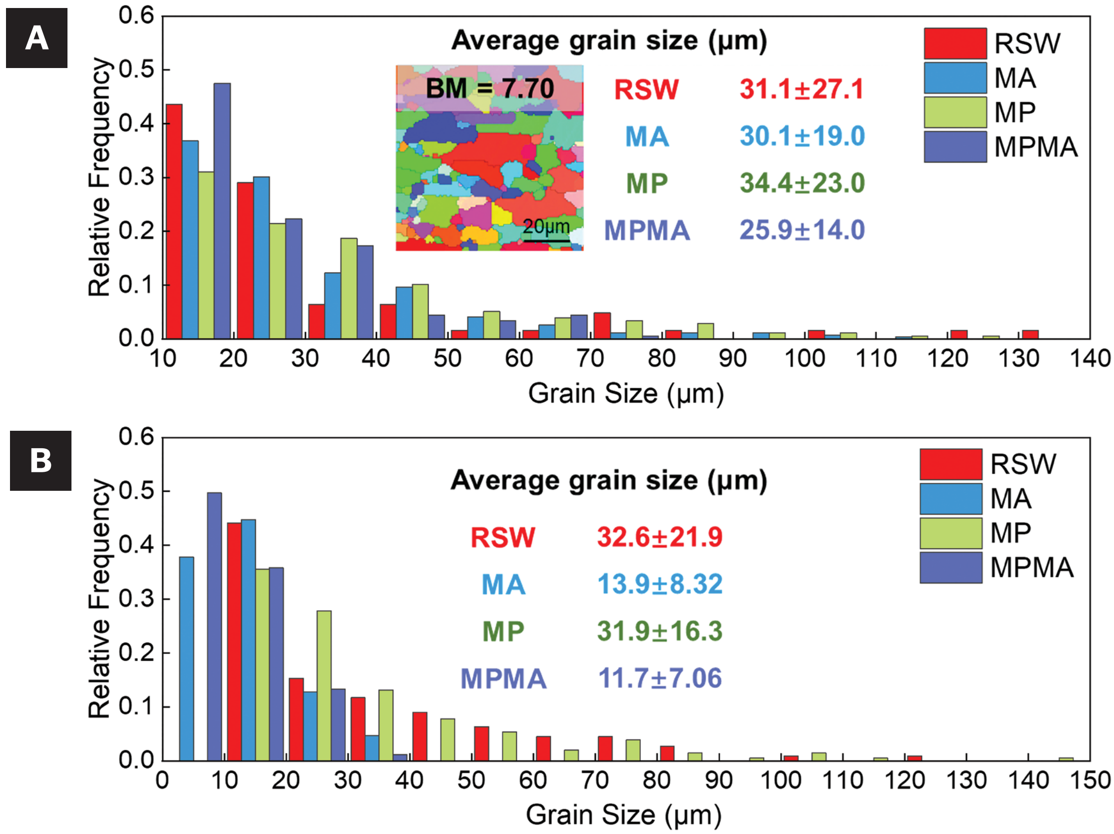

Fig. 8 — Grain width distribution (in equivalent circle diameter): A — Grain width of CGZ; B — grain width of EGZ.

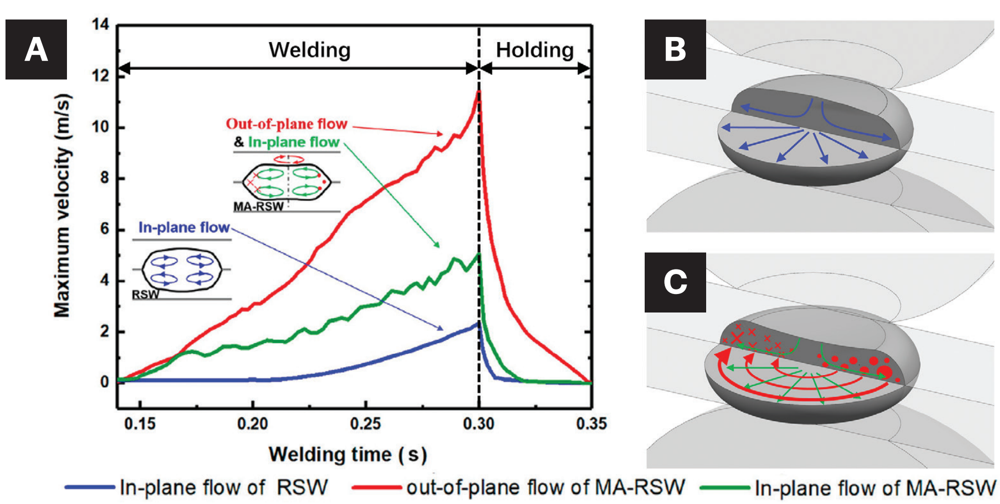

Fig. 9 — Schematic diagrams of flow patterns within the nugget of RSW and MA-RSW: A — Simulation curve of the flow velocity within the nugget as a function of welding time, with a welding time of 0.3 s (Ref. 31); B — RSW exhibits only in-plane flow patterns; C — MA-RSW combines in-plane and out-of-plane flow patterns.

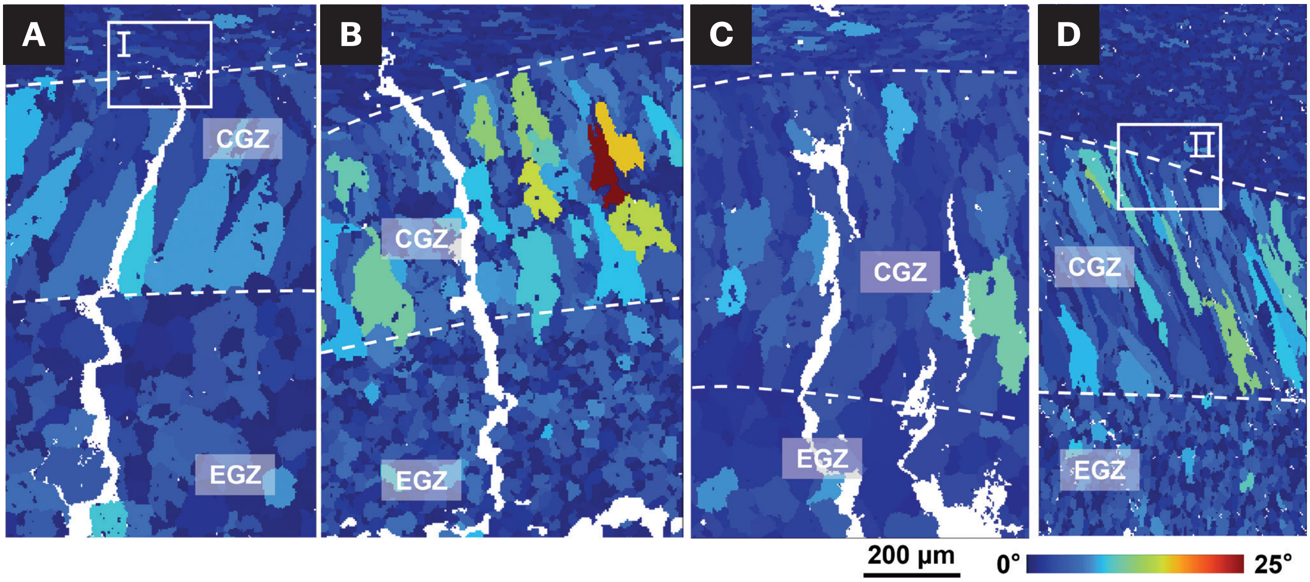

Fig. 10 — Grain orientation spread (GOS) map: A — RSW; B — MA-RSW; C — MP-RSW; D — MPMA-RSW.

equiaxed grains was not pronounced. However, it can also be observed that RSW has the highest proportion of fine grains in CGZ, and the average grain width of its CGZ was similar to that of MA-RSW. Yet, visually, the grains in the CGZ of RSW appear much coarser. This phenomenon is associated with the coarse grains in RSW occupying a larger area, which results in a reduced total grain count in that region. The average grain width was decreased due to the inclusion of a relatively higher number of small grains in the statistical analysis, leading to a larger standard deviation of grain widths in the CGZ of RSW.

There was a notable refinement of the grains in the EGZ for both MA-RSW and MPMA-RSW under the external magnetic field, as shown in Figs. 7B and D and Fig. 8B. Meanwhile, when comparing RSW and MPMA-RSW, no significant differences were observed in the grain size and morphology of their EGZ. These results may suggest that the external magnetic field and the high-speed flow it generates within the nugget substantially impact the grain morphology in the EGZ. The high-speed flow in the MA-RSW and MPMA-RSW nugget facilitated the breaking of dendrites during the solidification process, thereby increasing the number of nucleation sites (Ref. 33). Unlike CGZ, the solidification mode of the EGZ was closer to simultaneous solidification. Under the influence of an external magnetic field, with more nucleation sites nucleating, the EGZ in MA-RSW and MPMA-RSW exhibited significant refinement (Ref. 34). However, the multipulse technique alone appears insufficient to influence the nucleation and growth processes during solidification.

The Influence of the CGZ

Grain orientation spread (GOS) indicates the difference between each pixel in the grain and the average orientation in the grain (Ref. 35). A high GOS exhibits severe lattice distortion and a high dislocation density, while grains with a low GOS exhibit a uniform strain distribution (Ref. 36). The GOS plotted corresponding to Fig. 7 was separately extracted and presented in Fig. 10. Compared with RSW, MP-RSW decreased the GOS of the CGZ. It was evident that the GOS values of the CGZ were consistently higher than those of the EGZ, implying a larger dislocation density and suggesting the presence of higher residual stress, which may be another significant factor contributing to the exacerbation of crack propagation in the CGZ. Possibly due to the intense effect of electromagnetic stirring, MA increased the GOS of the CGZ. However, repetitive remelting reduces the stress in the CGZ of MPMA, which may be a key factor in reducing cracking.

From Fig. 7, it can be observed that cracks propagated through the grain boundaries in the CGZ. A higher grain boundary angle leads to an increased crack sensitivity (Ref. 37). From the grain boundary angle distribution in the CGZ region presented in Fig. 11, it was evident that the CGZ grain boundary angle of MA-RSW exhibited a reduction of 20.8% when compared to RSW, while the MPMA-RSW grain boundary angle showed a decrease of 16.4% in comparison to MP-RSW. This observation suggests that electromagnetic stirring can diminish the grain boundary angle. Given the minimal variation in grain size depicted in Fig. 8, it was more probable that this reduction was primarily influenced by solidification rate and molten metal flow.

The Formation of Hot Cracks

As shown in Fig. 12, EBSD analyses were performed on two typical crack regions, marked by Roman numerals I and II in Figs. 10A and D. Cracks are present in both the CGZ and HAZ of the two regions. However, in RSW, the Kernel Average Misorientation (KAM) values near the CGZ cracks are lower, while those cracks near the HAZ are higher, as shown in Fig. 12C. In MPMA-RSW, the KAM values near the CGZ cracks are higher, whereas the KAM values near the independent cracks within the HAZ, which are not connected to the CGZ, are lower, as shown in Fig. 12D. High KAM values are indic-

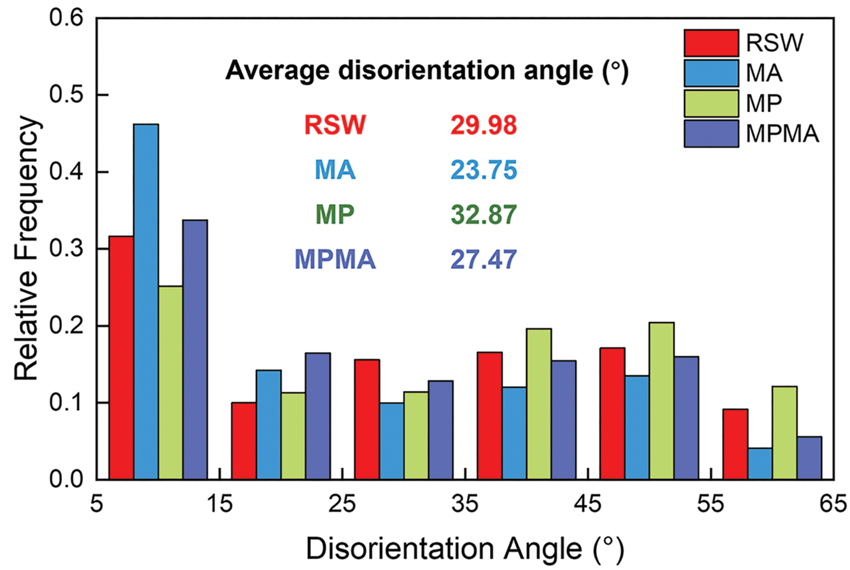

Fig. 11 — The disorientation angle distribution of CGZ.

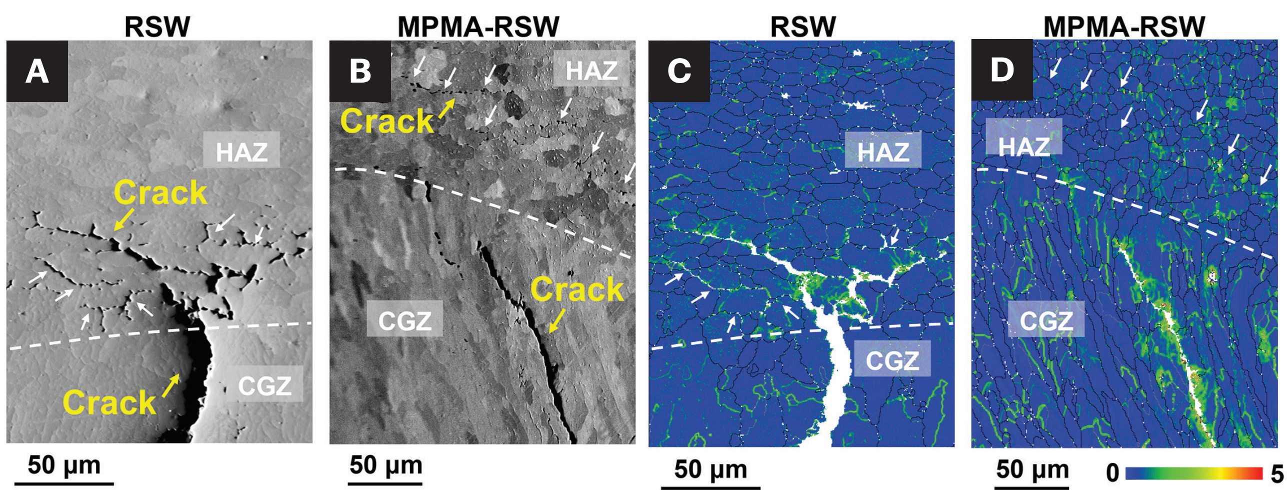

Fig. 12 — Crack initiation locations: A and B — are the forescatter detector (FSD) corresponding to the regions I~II marked in Figs. 10A and D; C and D — are the KAM maps of A and B.

ative of greater plastic strain in that particular location. As illustrated in Fig. 12C, cracks in the RSW process have been observed to extend from the CGZ to the HAZ, resulting in substantial plastic strain in the vicinity of the HAZ part of the cracks that connect the HAZ and CGZ. In contrast, the independent HAZ cracks (indicated by white arrows) do not exhibit significant plastic strain concentration in both processes. Figure 12D demonstrates that the plastic strain in proximity to the CGZ cracks in MPMA-RSW is higher, likely attributable to a more stringent constraint at that location during crack formation. This finding also suggests that the CGZ of MPMA-RSW exhibits higher crack resistance compared to that of RSW, a subject that will be further examined in the subsequent sections.

As depicted in Fig. 13, an elemental analysis was conducted on the HAZ and the CGZ at the crack tip. Firstly, from Fig. 13A, it can be observed that there was a significant segregation at the grain boundaries in the HAZ, while segregation in the CGZ occurred both at the grain boundaries and within the grains. From Figs. 13C–F, it was evident that the matrix around the segregated regions had a lower aluminum content and higher concentrations of alloying elements such as Zn, Mg, and Cu. Since these alloying elements formed low-melting eutectics, these regions were prone to crack formation. Cracks predominantly occurred along grain boundaries, where reduced concentrations of alloying elements suggested that the low-melting eutectics in these areas liquefied during cracking and flowed under stress (Ref. 38).

As shown in Fig. 12, unlike the liquefaction cracks reported in previous research (Ref. 18), the HAZ cracks in this study were not filled, indicating that the CGZ solidified when HAZ cracks formed. The liquid film formed by low-melting eutectics was pulled apart by tensile stress, resulting in hot cracks. According to the above analysis, the CGZ grain

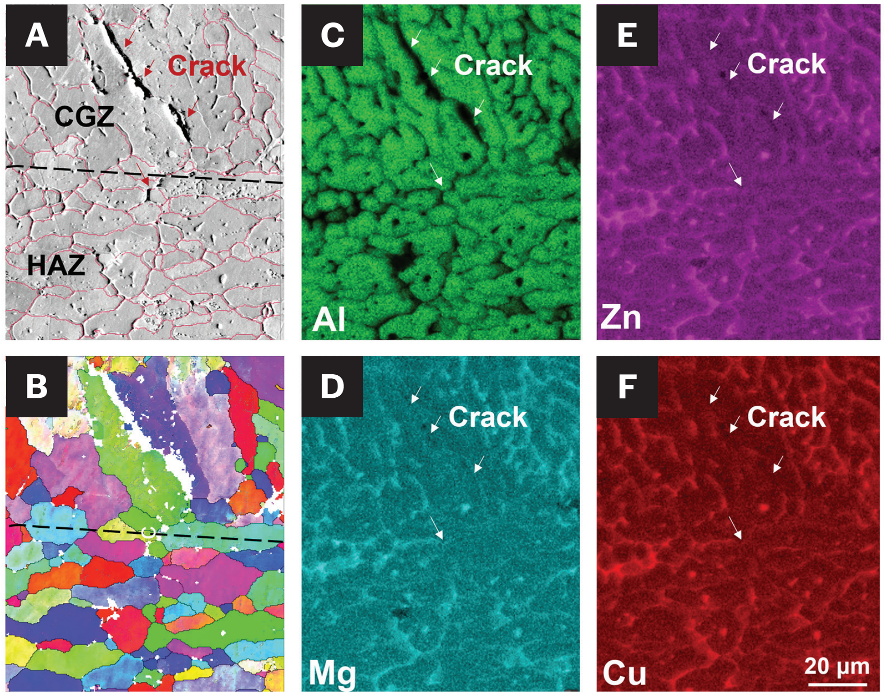

Fig. 13 — Elemental analysis at the crack initiation: A — FSD image with the combined image of grain boundaries marked in red; B — IPF-Z image; C–F — elemental distribution.

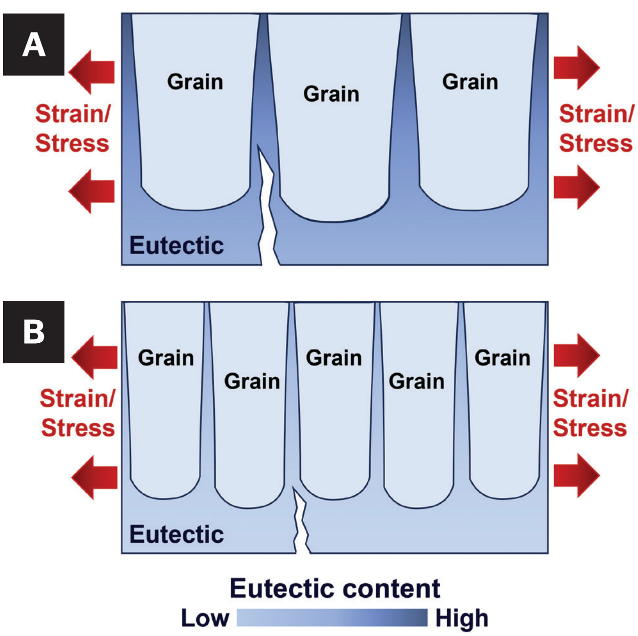

Fig. 14 — Mechanism of crack resistance enhancement by grain refinement in CGZ: A — Schematic of coarse columnar grains in RSW; B — elongated columnar grains in MPMA-RSW under vertical tensile stress.

experienced significant stress and deformation, and the low-melting eutectics along the long longitudinal grain boundaries in the CGZ became weak sites, which may be a key factor in the formation of intergranular hot cracks in this zone, as Fig. 14A shows. However, the CGZ in MPMA-RSW exhibits higher crack resistance, which may be attributed to the lower content of low-melting-point eutectics at the grain boundaries. This low content of eutectics could be closely related to the finer grains in its CGZ. The combined effects of various factors caused the segregation of alloying elements at the grain boundaries. First, due to the relatively low activation energy for grain boundary diffusion, the diffusion rate of low-melting-point eutectic elements at the grain boundaries is relatively fast (Ref. 39). Besides, differing equilibrium coefficients between solid and liquid phases drive solute redistribution, while non-equilibrium solidification further concentrates solute elements at grain boundaries (Ref. 40). Consequently, finer grains expel less eutectic matter and have a larger grain boundary area, which can significantly reduce the content of low-melting-point eutectics at the grain boundaries. Additionally, the repeated heating and cooling cycles of the multipulse process may inhibit the precipitation of low-melting-point eutectics (Ref. 41), making the content of eutectics lower at the grain boundaries in MPMA-RSW. As shown in Fig. 14, the nugget center has large tensile residual stress after welding (Ref. 42), and the low content eutectics at the grain boundaries could increase the grain boundaries' strength and enhance the crack resistance.

In addition, the refined grains produce more grain boundaries. The cracks will be deflected when they meet the grain boundaries in the crack growth process, which increases the resistance of crack growth and thus improves the crack resistance of the material (Ref. 43). At the same time, grain refinement can disperse the stress concentration of crack tip, reduce the stress intensity factor of crack tip, and inhibit the crack growth (Ref. 44).

Conclusions

This study investigated the RSW optimization process for 2.8 mm hot-stamped AA7075 aluminum alloy. Conventional RSW, RSW using an external magnetic field (MA-RSW) or multipulse current parameter (MP-RSW), and a combination of external magnetic field and multipulse current (MPMA-RSW) were employed for optimization and comparison. The nugget appearance, microstructure, and crack propagation were investigated in this part successively, and the following conclusions can be drawn:

1. MA-RSW could effectively inhibit porosity defects through electromagnetic stirring. In MA-RSW, unsymmetrical nugget growth was mitigated, with a notable 13.4% increase in nugget diameter alongside an 18.1% reduction in thickness. By inducing rapid circumferential flow and a low solidification rate, electromagnetic stirring in MA significantly reduced the grain size of EGZ by 57.4%.

2. MP-RSW, by repetitively heating the nugget, reduced the cooling rate and effectively suppressed pore defects. However, the hot cracking defects and the unsymmetric nugget growth remained, with minimal alteration to the grain sizes of EGZ and CGZ.

3. MPMA-RSW, leveraging the combined effects of both processes, demonstrated a 12.9% increase in nugget diameter and an 8.84% decrease in thickness. Moreover, it substantially reduced the grain sizes of CGZ by 24.7% and EGZ by 63.3%. This combined approach resulted in comprehensive defect suppression and exhibited the lowest defect severity.

4. Cracks were attributed to low-melting-point eutectic alloy in the grain boundaries and stress. CGZ, characterized by longer grain boundaries and higher stress, notably contributed to crack propagation. MPMA-RSW effectively reduced the CGZ area and the grain size and stress in the CGZ, consequently decreasing the incidence of cracking.

The MPMA-RSW process presented promising application prospects in welding AA7075. A comparative analysis of the four process combinations revealed that the MPMA-RSW nugget exhibited notably fewer defects and a diminished propensity for hot cracking. This observation underscored the heightened feasibility of this method. Consequently, the MPMA-RSW process emerged as a promising avenue for application in the RSW of AA7075.

Acknowledgments

The authors would like to acknowledge the financial support of the National Natural Science Foundation of China (Grant Nos. 52025058 and 52205396), the Young Elite Scientists Sponsorship Program by CAST (Grant No. 2022QNRC001), the Shanghai Rising-Star Program (Grant No. 23QB1405700), and the Guangxi Science and Technology Major Program (Grant No. AA23062069).

In addition, the authors would like to acknowledge the financial support of the National Natural Science Foundation of China (Grants 52025058, 52205396), National Defense Basic Scientific Research Program of China (Grant JCKY2021203B074), the Young Elite Scientists Sponsorship Program by CAST (Grant 2022QNRC001), the Shanghai Rising-Star Program (Grant 23QB1405700), and the Guangxi Science and Technology Major Program (Grant AA23062069).

References

1. Yuan, Y., Wu, Z., Chen, K., Liu, H., Huang, H., and Li, Y. 2025. Effects of plunge depth on macro-/microstructure and mechanical properties of refill friction stir spot welded 2195-T6 Al–Li alloy. *Journal of Materials Research and Technology* 35: 6026–6041. DOI: 10.1016/j.jmrt.2025.02.046

2. Zhang, B., Ma, Y., Yu, F., Liu, Y., Zhou, E., Fan, Z., Ge, E., Li, Y., and Lin, Z. 2024. Strengthening flat-die friction self-pierce riveting joints via manipulating stir zone geometry by tailored rivet structures. *International Journal of Machine Tools and Manufacture* 203: 104223. DOI: 10.1016/j.ijmachtools.2024.104223

3. Dobosy, Á., Gáspár, M., and Török, I. 2018. Resistance spot welding of 7075 aluminium alloy. *Vehicle and Automotive Engineering* 2: 679–693. DOI: 10.1007/978-3-319-75677-6_58

4. Sokoluk, M., Cao, C., Pan, S., and Li, X. 2019. Nanoparticle-enabled phase control for arc welding of unweldable aluminum alloy 7075. *Nature Communications* 10. DOI: 10.1038/s41467-018-07989-y

5. Ma, Y., Yang, B., Hu, S., Shan, H., Geng, P., Li, Y., and Ma, N. 2022. Combined strengthening mechanism of solid-state bonding and mechanical interlocking in friction self-piercing riveted AA7075-T6 aluminum alloy joints. *Journal of Materials Science & Technology* 105: 109–121. DOI: 10.1016/j.jmst.2021.07.026

6. Liu, H., Chen, K., Wu, Z., Li, Y., Yoshiaki, M., and Fujii, H. 2025. A novel multi-stage pressuring strategy to fabricate sound high carbon steel joints in rotary friction welding. *Journal of Manufacturing Processes* 133: 957–968. DOI: 10.1016/j.jmapro.2024.11.101

7. Zhang, Z., Li, X., Zhu, D., and Qu, S. 2022. Microstructural and mechanical characteristics of 7075-t6 aluminum alloy joint by double wire pulsed cold metal transition welding. *Journal of Physics: Conference Series* 2383: 012103. DOI: 10.1088/1742-6596/2383/1/012103

8. Liu, T., Mu, Z., Hu, R., and Pang, S. 2019. Sinusoidal oscillating laser welding of 7075 aluminum alloy: Hydrodynamics, porosity formation and optimization. *International Journal of Heat and Mass Transfer* 140: 346–358. DOI: 10.1016/j.ijheatmasstransfer.2019.05.111

9. Hu, Y., Wu, S., Guo, Y., Shen, Z., Korsunsky, A. M., Yu, Y., Zhang, X., Fu, Y., Che, Z., Xiao, T., Lozano-Perez, S., Yuan, Q., Zhong, X., Zeng, X., Kang, G., and Withers, P. J. 2022. Inhibiting weld cracking in high-strength aluminium alloys. *Nature Communications* 13. DOI: 10.1038/s41467-022-33188-x

10. Shen, Q., Li, Y., Lin, Z., and Chen, G. 2011. Impact of external magnetic field on weld quality of resistance spot welding. *Journal of Manufacturing Science and Engineering* 133. DOI: 10.1115/1.4004794

11. Qi, L., Li, Z., Zhang, Q., Wu, W., Huang, N., and Li, Y. 2021. Electromagnetic stirring control for resistance spot welding of SiCp/Al composites. *Journal of Manufacturing Processes* 68: 1271–1279. DOI: 10.1016/j.jmapro.2021.06.048

12. Qi, L., Zhang, Q., Ma, Y., Xu, Y., Han, X., and Li, Y. 2021. A comparative study on mechanical performance of traditional and magnetically assisted resistance spot welds of A7N01 aluminum alloy. *Journal of Manufacturing Processes* 66: 133–144. DOI: 10.1016/j.jmapro.2021.04.006

13. Qiaobo, F., Ma, Y., Zhang, Q., David, S., and Li, Y. 2024. Quality improvement in resistance spot welding of H1000 austenitic stainless steel using an external magnetic field. *Science and Technology of Welding and Joining* 30(2). DOI: 10.1177/13621718241308375

14. Xia, Y.-J., Song, Q., Yi, B., Lyu, T., Sun, Z., and Li, Y. 2025. Improving out-of-distribution generalization for online weld expulsion

inspection using physics-informed neural networks. *Welding in the World* 69: 1309–1322. DOI: 10.1007/s40194-025-01950-6

15. Li, Z., Huo, Z., Zhao, X., Xia, Y.-J., Huang, S., Liu, H., Xi, X., and Li, Y. 2024. Effect of external magnetic field on microstructures and mechanical properties of Ti-2Al-1.5Mn titanium alloy resistance spot welds. *Journal of Manufacturing Processes* 124: 1273–1284. DOI: 10.1016/j.jmapro.2024.07.010

16. Li, Z., Zhang, D., Chen, R., Wang, S., Xia, Y., Lou, M., Li, Y. 2024. Improving weldability of press hardened steel through combining stepped current pulse and magnetically assisted resistance spot welding process. *Journal of Manufacturing Science and Engineering* 146(2): 021007. DOI: 10.1115/1.4063904

17. Sigler, D. R., and Karagoulis, M. J. 2018. Weld schedule for resistance spot welding of aluminum alloy workpieces. US Patent 20130048613A1, filed December 2, 2011, and issued May 15, 2018.

18. Deng, L., Li, Y., Carlson, B. E., and Sigler, D. 2018. Effects of electrode surface topography on aluminum resistance spot welding. *Welding Journal* 97(4): 120-s to 132-s. DOI: 10.29391/2018.97.011

19. Sigler, D. R., Carlson, B. E., and Karagoulis, M. J. 2019. Multistage resistance spot welding method for workpiece stack-up having adjacent steel and aluminum workpieces. US Patent 20170106466A1, filed October 14, 2015, and issued April 2, 2019.

20. Sigler, D. R., and Karagoulis, M. J. 2014. Cutting tool for forming and re-forming welding electrodes with contoured faces. US Patent 20130008295A1, filed September 14, 2012, and issued September 16, 2014.

21. AWS D8.2M:2017, *Specification for Automotive Weld Quality — Resistance Spot Welding of Aluminum*. Miami, Fla.: AWS.

22. Huang, S., Lu, R., Lou, M., Lv, T., Yao, J., and Li, Y. 2024. Effect of oscillation parameters on adjustable-ring mode (ARM) laser beam welding of aluminum alloys. *Journal of Manufacturing Processes* 113: 307–318. DOI: 10.1016/j.jmapro.2024.01.060

23. Yi, H., Qi, L., Luo, J., and Li, N. 2019. Hole-defects in soluble core assisted aluminum droplet printing: Metallurgical mechanisms and elimination methods. *Applied Thermal Engineering* 148: 1183–1193. DOI: 10.1016/j.applthermaleng.2018.12.013

24. Deng, L., Li, Y., Cai, W., Haselhuhn, A. S., and Carlson, B. E. 2020. Simulating thermoelectric effect and its impact on asymmetric weld nugget growth in aluminum resistance spot welding. *Journal of Manufacturing Science and Engineering* 142. DOI: 10.1115/1.4047243

25. Ochieng, A. O., Megahed, T. F., Ookawara, S., and Hassan, H. 2022. Comprehensive review in waste heat recovery in different thermal energy-consuming processes using thermoelectric generators for electrical power generation. *Process Safety and Environmental Protection* 162: 134–154. DOI: 10.1016/j.psep.2022.03.070

26. Testbook. Fermi Energy: Learn its Formula, How to Calculate it, Fermi Level, and Application. Retrieved January 8, 2025, from *testbook.com/physics/fermi-energy*.

27. Hu, S., Haselhuhn, A. S., Ma, Y., Li, Y., Carlson, B. E., and Lin, Z. 2021. Sensitivity of dissimilar aluminum to steel resistance spot welds to weld gun deflection. *Journal of Manufacturing Processes* 68: 534–545. DOI: 10.1016/j.jmapro.2021.05.059.

28. Xia, Y. J., Lv, T., Ghassemi-Armaki, H., Li, Y., and Carlson, B.E. 2023. Collaborative simulation of nugget growth and process signals for resistance spot welding. *Welding in the World* 67: 1377–1392. DOI: 10.1007/s40194-023-01489-4

29. Li, Y., Li, Y., Shen, Q., and Lin, Z. 2013. Magnetically assisted resistance spot welding of dual-phase steel. *Welding Journal* 92(4): 124-s to 132-s.

30. Li, Y., Zhang, Q. X., Qi, L., and David, S. A. 2018. Improving austenitic stainless steel resistance spot weld quality using external magnetic field. *Science and Technology of Welding and Joining* 23: 619–627. DOI: 10.1080/13621718.2018.1443997

31. Qi, L., Zhang, Q., Niu, S., Chen, R., and Li, Y. 2021. Influencing mechanism of an external magnetic field on fluid flow, heat transfer and microstructure in aluminum resistance spot welding. *Engineering Applications of Computational Fluid Mechanics* 15: 985–1001. DOI: 10.1080/19942060.2021.1938684

32. Cantor, B., and O'Reilly, K. 2016. *Solidification and casting*. Boca Raton, Fla.: CRC Press.

33. Wen, J., Liu, Y., Huang, Y., and Zhao, Y. 2023. Effects of electromagnetic stirring and subsequent homogenization treatment on the microstructure and mechanical properties of Al70Zn10Mg-10Cu5Si5 multi-component alloy. *Journal of Alloys and Compounds* 960: 170725. DOI: 10.1016/j.jallcom.2023.170725

34. Metan, V., Eigenfeld, K., Räbiger, D., Leonhardt, M., and Eckert, S. 2009. Grain size control in Al–Si alloys by grain refinement and electromagnetic stirring. *Journal of Alloys and Compounds* 487: 163–172. DOI: 10.1016/j.jallcom.2009.08.032

35. Cross, A. J., Prior, D. J., Stipp, M., and Kidder, S. 2017. The recrystallized grain size piezometer for quartz: An EBSD-based calibration. *Geophysical Research Letters* 44: 6667–6674. DOI: 10.1002/2017gl073836

36. Kar, A., Suwas, S., and Kailas, S. V. 2019. Multi-length scale characterization of microstructure evolution and its consequence on mechanical properties in dissimilar friction stir welding of titanium to aluminum. *Metallurgical and Materials Transactions A* 50: 5153–5173. DOI: 10.1007/s11661-019-05409-4

37. Wang, N., Mokadem, S., Rappaz, M., and Kurz, W. 2004. Solidification cracking of superalloy single- and bi-crystals. *Acta Materialia* 52: 3173–3182. DOI: 10.1016/j.actamat.2004.03.047

38. Chandra, S., Tan, X., Narayan, R. L., Wang, C., Tor, S. B., and Seet, G. 2021. A generalised hot cracking criterion for nickel-based superalloys additively manufactured by electron beam melting. *Additive Manufacturing* 37. DOI: 10.1016/j.addma.2020.101633

39. Boettinger, W. J., and Banerjee, D. K. 2014. "7 – Solidification." In *Physical Metallurgy*, 5th Edition, edited by Laughlin, D. E., and Hono, K., 639–850. Amsterdam: Elsevier. DOI: 10.1016/B978-0-444-53770-6.00007-1

40. Jie, W. 2001. Solute redistribution and segregation in solidification processes. *Science and Technology of Advanced Materials* 2: 29–35. DOI: 10.1016/S1468-6996(01)00022-5

41. Li, Y., Long, H., Wei, B., Zhou, J., and Lin, F. 2024. Multiple preheating processes for suppressing liquefaction cracks in IN738LC superalloy fabricated by electron beam powder bed fusion (EB-PBF). *Materials* 17: 5667. DOI: 10.3390/ma17225667

42. Khanna, S., and Long, X. 2008. Residual stresses in resistance spot welded steel joints. *Science and Technology of Welding and Joining* 13(3): 278–288. DOI: 10.1179/174329308X283884

43. Chen, Y. Q., Pan, S. P., Zhou, M. Z., Yi, D. Q., Xu, D. Z., and Xu, Y. F. 2013. Effects of inclusions, grain boundaries and grain orientations on the fatigue crack initiation and propagation behavior of 2524-T3 Al alloy. *Materials Science and Engineering: A* 580: 150–158. DOI: 10.1016/j.msea.2013.05.053

44. Li, J., Wang, Z., Zhang, N., Shi, T., Gilbert, E.P., Chen, G., and Qian, G. 2024. Crack-tip plasticity mediated grain refinement and its resisting effect on the fatigue short crack growth. *International Journal of Plasticity* 181: 104102. DOI: 10.1016/j.ijplas.2024.104102

ZHUORAN LI, **JIAXUAN CHEN**, **JORDAN QUEVAL**, **CHANGMING QIAN**, **YUJUN XIA**, and **YONGBING LI** (*xyjdbgt6509@sjtu.edu.cn*) are with Shanghai Key Laboratory of Digital Manufacture for Thin-walled Structures, State Key Laboratory of Mechanical System and Vibration, School of Mechanical Engineering, Shanghai Jiao Tong University, Shanghai, China. **ZHENKE TENG** and **JASON BROWN** are with Global Manufacturing Engineering, General Motors Global Technical Center, Warren, Mich.